

Quantum-limited traveling-wave parametric amplifier based on DUV lithography-defined planar structures

Hao Li,^{1,2,3,*} Marco Scigliuzzo,^{1,2,3,*†} Evgenii Guzovskii,^{1,2,3,*}
Seog-Tae Han,⁴ Kyungho Han,⁴ and Tobias J. Kippenberg^{1,2,3,‡}

¹*Institute of Physics, Swiss Federal Institute of Technology Lausanne (EPFL), Lausanne, Switzerland.*

²*Institute of Electrical and Micro Engineering (IEM), EPFL, CH-1015 Lausanne, Switzerland*

³*Center for Quantum Science and Engineering, Swiss Federal Institute of Technology Lausanne (EPFL), Lausanne, Switzerland.*

⁴*WithWave Co.,Ltd., Quantum & Space technologies, Yongin, Republic of Korea.*

The relentless scaling of classical microelectronics has been enabled by the precision and reproducibility of deep-ultraviolet (DUV) optical lithography. Implementing large-scale superconducting quantum processors will require cryogenic microwave components that follow a similarly scalable fabrication path. This need is particularly acute for high circuit-density devices such as traveling-wave parametric amplifiers (TWPAs), where recent implementations have demonstrated high gain, broad bandwidth, high saturation power, and near-quantum-limited noise, but trade-offs between footprint, insertion loss, and scalable integration remain. Here, we demonstrate a four-wave-mixing TWPA fabricated via a hybrid scheme that combines DUV-defined planar circuit elements with electron-beam-patterned Josephson junctions, constituting a first step toward fully scalable manufacturing. The device combines a compact footprint with broadband gain from 3 to 11 GHz and an average 1 dB compression point of -102 dBm. By using planar capacitors to reduce loss, it operates near the quantum limit, with added noise near 0 and 1.5 photons above the standard quantum limit and an average of 0.4 photons in the 4 to 8 GHz band. The phase-matching stopband remains narrow, with a bandwidth of 43 MHz, consistent with resonator-frequency variation below 1% and indicative of the uniformity enabled by DUV lithography. These results show that DUV-defined planar elements can enable compact, low-loss, near-quantum-limited TWPAs and provide a promising route toward high-density cryogenic microwave hardware for large-scale quantum systems.

High-fidelity single-shot readout of superconducting quantum processors requires the amplification of weak microwave signals, often containing only a few photons, above the noise floor of room-temperature detectors [1]. To maximize the signal-to-noise ratio, the first-stage amplifier should ideally operate at the standard quantum

limit [2]. While resonant Josephson parametric amplifiers (JPAs) have successfully fulfilled this role in many fundamental experiments [3, 4], their resonant nature imposes a limited gain-bandwidth product [5, 6] and low saturation power [7]. These constraints become a major bottleneck for frequency-multiplexed readout, which is essential for scaling superconducting quantum processors.

Traveling-wave parametric amplifiers (TWPAs) overcome these limitations by using nonlinear transmission lines [8, 9] instead of a resonant cavity. The most widely studied implementations rely on four-wave mixing in nonlinear transmission lines, with the nonlinearity provided either by Josephson junctions [10–12] or kinetic inductance [13]. More recently, three-wave mixing schemes have also been developed using DC-biased high-kinetic-inductance waveguides [14], rf-SQUIDs [15, 16], and SNAIL arrays [17, 18]. Continued efforts to improve TWPA performance have led to major advances, including nonlinearity engineering [19, 20] and the suppression of unwanted higher-order mixing processes [21].

Despite this rapid progress, compact integration remains a major challenge. Recent TWPA implementations achieve very low added noise and insertion loss [22], but still rely on centimeter-scale chips. While promising results can be achieved by eliminating resonant phase matching [23], resonantly phase-matched devices have the advantage of a narrower power-independent stopband which simplifies the design and operation of the TWPA. The integration of the phase-matching resonators into a compact layout, however, remains a significant challenge. In large-scale cryogenic quantum hardware, significant footprints limit the circuit density and complicate packaging through the appearance of spurious box modes. Addressing these constraints is increasingly important as TWPAs are emerging not only as readout amplifiers, but also as useful sources of nonclassical microwave radiation [24–26].

Here, we present a compact resonantly phase-matched TWPA architecture that addresses this footprint-performance trade-off. Using a hybrid wafer-level fabrication process, with DUV lithography for linear circuit elements and electron-beam lithography for the Josephson junctions, we realize a device with individual resonator footprints of $\sim 0.02 \text{ mm}^2$ and a chip of $6.6 \times 6.6 \text{ mm}^2$, much smaller than the field size of our DUV reticle.

Importantly, this approach preserves sub-dB insertion

* These authors contributed equally.

*† These authors contributed equally.; marco.scigliuzzo@epfl.ch

‡ tobias.kippenberg@epfl.ch

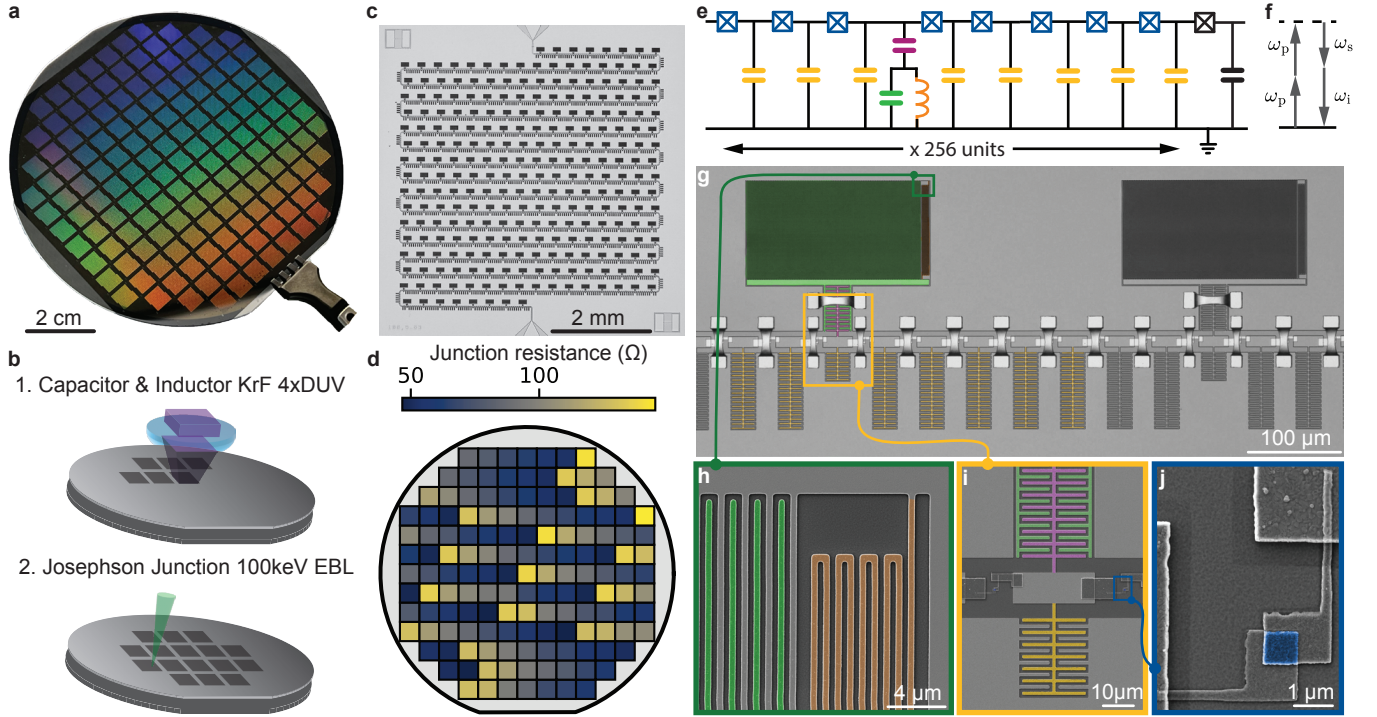


FIG. 1. Wafer-scale manufacturing of near quantum-limited Josephson traveling-wave parametric amplifier. **a**, the TWPA is realized on a 100 mm wafer, hosting 145 individual chips. The colors arise from the interference of scattered light by circuit features comparable to the optical wavelength. **b**, the core fabrication process relies on two primary lithography steps. Deep-ultraviolet (DUV) lithography (utilizing a 4x magnification mask) defines the waveguide capacitors, resonator capacitors, and meandered inductors. Electron-beam lithography (EBL) is subsequently used to define the Josephson junctions (JJs). The process is completed with junction patches and air-bridges to connect the ground planes (not shown). **c**, optical micrograph of a single TWPA chip post-dicing. **d**, room-temperature resistance mapping of single JJs, measured on test structures comprising 10- or 11-junction arrays. Junction dimensions are swept across nine discrete values. **e**, equivalent circuit schematic of a single TWPA unit cell, consisting of eight JJs and a phase-matching resonator. This unit cell is cascaded 256 times along the transmission line. **f**, amplification relies on a four-wave mixing process, wherein two pump photons at frequency ω_p are converted into a signal photon at ω_s and an idler photon at ω_i . **g**, false-color scanning electron microscope (SEM) micrograph of a unit cell. Highlighted components include the phase-matching resonator capacitor (green) and inductor (orange), detailed further in **h**. **i**, Close-up of the resonator coupling capacitor (purple) and the capacitance to ground (yellow). **j**, SEM micrograph detailing the Josephson junctions (blue).

loss, as required for compatibility with high-coherence superconducting qubit platforms. Moreover, the observation of a narrow phase-matching stopband is consistent with small resonator-frequency variation, estimated to be below 1%. The amplifier provides gain across 3 to 11 GHz band, excluding a gap related to the phase-matching features, while maintaining an average 1 dB compression point of -102 dBm between 4 and 8 GHz. Our TWPA adds on average 0.4 photons/second/Hz above the quantum limit over the same frequency range, positioning this planar architecture as a promising route toward scalable multiplexed readout.

Implementation of compact planar TWPA

We fabricate the TWPAs on a 100 mm silicon wafer as shown in Fig. 1a using sputtered niobium for the ground plane, and evaporated aluminum for the Josephson junc-

tions and the air bridges. The fabrication consists of the definition of the linear components (inductors and capacitors) on the 150 nm thick Niobium ground plane with DUV lithography (248 nm wavelength KrF laser, with a 4x reduction of the mask image). The lithography takes less than 10 minutes per wafer, including spin coating, post exposure bake and development of the photoresist. The ground plane etching is then performed using inductively coupled plasma reactive ion etching with chlorine chemistry. Electron-beam lithography (EBL) and shadow electron-beam evaporation of aluminum is subsequently used to define the Josephson junctions (see Fig. 1b). The process is completed with junction patches and air-bridges to connect the ground planes. An optical micrograph of a single TWPA chip post-dicing is shown in Fig. 1c. The chip dimensions are $6.6 \times 6.6 \text{ mm}^2$, which allows for small packaging and the absence of chip modes within the operation band. The junction's size is swept over 9 different values with a relative increment of

20%, as shown in the map of the room-temperature resistance of single JJs, reported in Fig. 1d. This mitigates the run to run variability in the critical current density of the junctions due to oxidation conditions and ensures devices with the desired JJ critical current are present on the wafer.

The full amplifier chain consists of 256 unit cells, each containing 8 JJs and a phase-matching resonator, as shown in the equivalent circuit schematic of Fig. 1e. The amplification relies on a four-wave mixing process, wherein two pump photons at the frequency ω_p are converted into a signal photon at ω_s and an idler photon at ω_i , as shown in Fig. 1f. A false-color scanning electron microscope (SEM) micrograph of a unit cell is shown in Fig. 1g, where the phase-matching resonator's capacitor (green) and inductor (orange) are highlighted. A close-up of the resonator coupling capacitor (purple) and the capacitance to ground (yellow) are shown in Fig. 1i. Finally, a SEM micrograph detailing the Josephson junctions (blue) is shown in Fig. 1j.

To achieve a compact footprint and avoid the appearance of chip modes we minimize the pitch of the features of the resonator's inductor and capacitor to 800 nm, and to $2\ \mu\text{m}$ for the coupling capacitors. The junctions have a critical dimension of 250 nm for the contact pads, however the dimensions of the junction area are close to $1 \times 1\ \mu\text{m}^2$.

Amplification performance

Internal reflections and impedance mismatch between the TWPA and the $50\ \Omega$ environment can lead to ripples in the gain profile [27], which in turn cause ripples in the added noise. To minimize these effects, we realize a package based on small PCBs with short transmission lines as shown in Fig. 2c. To shift the cavity and chip modes of packaged assembly beyond the TWPA's operating frequency range, a vacuum pocket with optimized dimensions is added beneath the chip. Furthermore, custom-designed K-band connectors are employed to enhance the grounding interface between the connectors and the PCBs.

The sample packaging is characterized at room temperature by measuring the transmittance and reflectance of the package containing a straight gold coplanar waveguide replacing the TWPA chip, reported in Fig. 2b. The reflection of the package is well below -20 dB up to 8 GHz, which is important for achieving low ripple in the gain and added noise of the amplifier.

In Fig. 2d we report the insertion loss of the TWPA without the pump, measured by comparing the transmission through the TWPA to the transmission of a bypass cable. The insertion loss is below 1 dB across the 3 to 8 GHz band, which is crucial for achieving quantum-limited noise performance [21, 26]. In Fig. 2e we report a detailed scan of the phase-matching stopband, highlighting the narrow 43 MHz rejection region. In both panels,

the continuous line represents a theoretical calculation of the transmission through TWPA. The circuit parameters for this calculation are drawn from a normal distribution with a standard deviation of 0.2% in the resonator's capacitor and the mean value to match the frequency of the stopband. We fit the phase delay of the transmitted signal referenced to the bypass cable to extract the speed of light in the transmission line of the TWPA using the simulated value of the capacitance to the ground obtaining an impedance of $58.5\ \Omega$.

In Fig. 2f we report the gain measured by comparing the output of the TWPA with the transmission through a bypass coaxial cable. The gain exceeds 10 dB in the 3 to 11 GHz range, except for a 600 MHz band around the pump frequency at 6.688 GHz where the propagation of either the signal or the idler is prohibited by the phase-matching stopband. The gain ripples vary between 5 and 10 dB, and are partially due to the impedance mismatch of the chain to the $50\ \Omega$ environment.

The continuous orange line represents the gain calculated in a harmonic balance circuit simulation [28] using circuit parameters extracted from finite element electromagnetic simulations of our design. Additionally, as mentioned above we introduce random variability to the frequency of the phase-matching resonators, to match the experimentally measured linewidth of the stopband which cannot be explained by the external coupling rate of the resonators at a single frequency alone.

In order to precisely calibrate the attenuation of the signal and the pump line we use a frequency tunable transmon overcoupled to a waveguide in a notch configuration (see Fig. 3a and inset). The frequency of the transmon is tuned with a superconducting coil biased with a DC current filtered at the 4K stage. The transmittance around the qubit resonance is measured at varying driving powers, and reported in Fig. 3b. At high probe powers the qubit is completely saturated while at lower powers the qubit response follows a Lorentzian. At resonance this gives the characteristic shape reported in Fig. 3c. These complex transmittances are globally fit as a function of probe power and frequency (solid black line), giving a primary estimator for the attenuation between the qubit reference plane and the output reference plane of the VNA. The extracted attenuation values within the qubit tunability range of 4 to 8 GHz are reported in Fig. 3d. The attenuation exhibits a linear frequency dependence in logarithmic scale, which is expected for the coaxial cables used in the measurement setup. We fit the extracted attenuation with a linear function (solid line) and use it to calibrate the power spectra measured with a spectrum analyzer in units of quanta per s per Hz. Measuring the power spectra with and without parametric pump (see Fig. 3e where we report the PSD with the pump on and pump off for the signal frequency of 5 GHz normalized to the input of the TWPA) we extract the added noise referred to the input of the TWPA (n_{add}), which is plotted in Fig. 3f, using

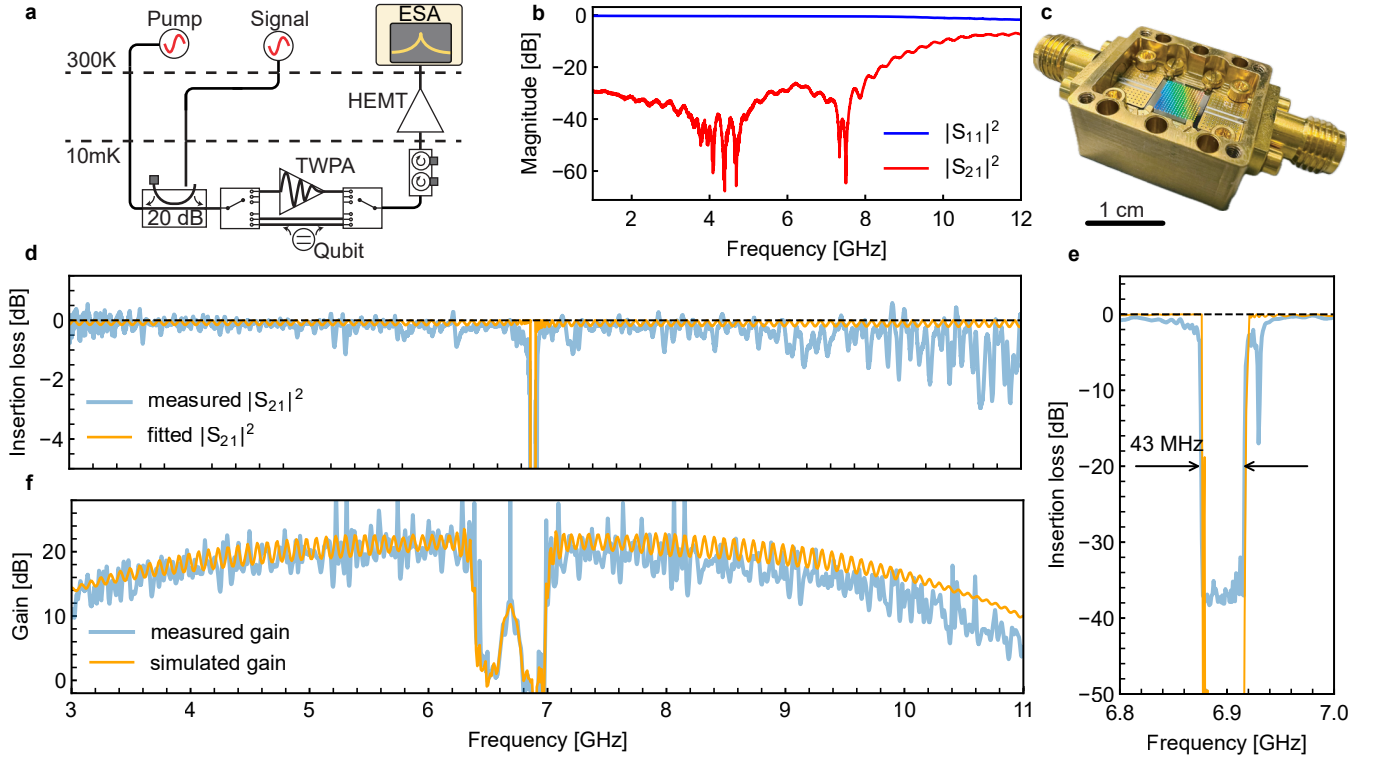


FIG. 2. **Performance characterization of the traveling-wave parametric amplifier.** **a**, Simplified schematic of the measurement setup. The TWPA is mounted on the mixing chamber stage of a dilution refrigerator, with the signal and the pump tone injected through a directional coupler. A bypass coaxial cable and a qubit directly coupled to the waveguide allow for direct transmission measurements without the amplifier and power calibration, respectively. **b**, Transmittance $|S_{21}|^2$ and reflectance $|S_{11}|^2$ of the sample packaging at room temperature for a gold straight CPW. **c**, Packaged TWPA without the box's lid. **d**, Insertion loss of the TWPA without the pump, measured by comparing the transmission through the TWPA with the bypass cable. **e**, A detailed scan of the phase-matching stopband, highlighting the narrow 43 MHz rejection region. The continuous line represents a theoretical fit to the propagation in the TWPA line. **f**, Gain profile measured by comparing the TWPA output with the transmission through the bypass coaxial cable. Around the pump frequency at 6.688 GHz, two regions of no gain are visible due to the phase-matching stopband. The continuous orange line represents the simulated gain using extracted parameters. Crucially, the ripples observed in the measured gain directly correlate with the impedance mismatch and package resonances characterized in panel **b**.

the following equation:

$$n_{\text{add}}^{\text{T}} = \left(\frac{N_{\text{on}} - N_{\text{off}}}{G_{\text{sys}}} + \frac{1}{2} \right) \frac{1}{G_{\text{T}}} - \frac{1}{2}, \quad (1)$$

where N_{on} is the PSD of the noise when the TWPA pump is on, N_{off} the noise PSD when the pump is off, G_{sys} is the gain of the readout chain after the TWPA, G_{T} is the parametric gain of the TWPA.

For given gain G the standard quantum limit of added noise for a phase insensitive amplifier can be calculated as $n_{\text{add}} = \frac{1}{2} \frac{G-1}{G}$. We can therefore calculate this limit (solid black line in Fig. 3f) for the measured gain of the TWPA and compare it to the added noise inferred from the measurement. The amplifier achieves an average added noise of 0.4 photons per second per Hz over the standard quantum limit in the 3.5 to 8 GHz range. The greyed-out band indicates the frequency range where the phase-matching stopband prohibits the propagation of either the signal or the idler, and is excluded from the average added-noise

calculation. Finally, we determine the signal-to-noise ratio improvement (SNRi) by subtracting the baseline SNR through a bypass cable from the amplified signal SNR (see Fig. 3g).

Power handling

Intermodulation products can severely degrade amplifier performance, particularly in frequency-multiplexed qubit readout schemes [29]. To establish the operational limits of our device, we systematically characterized its power handling capabilities.

The small-signal gain increases with pump power, reaching a maximum of approximately 20 dB at an incident pump power of -73 dBm (see Fig. 4a). However, the signal-to-noise ratio improvement (SNRi) peaks at a lower pump power. This divergence between maximum gain and maximum SNRi indicates the onset of para-

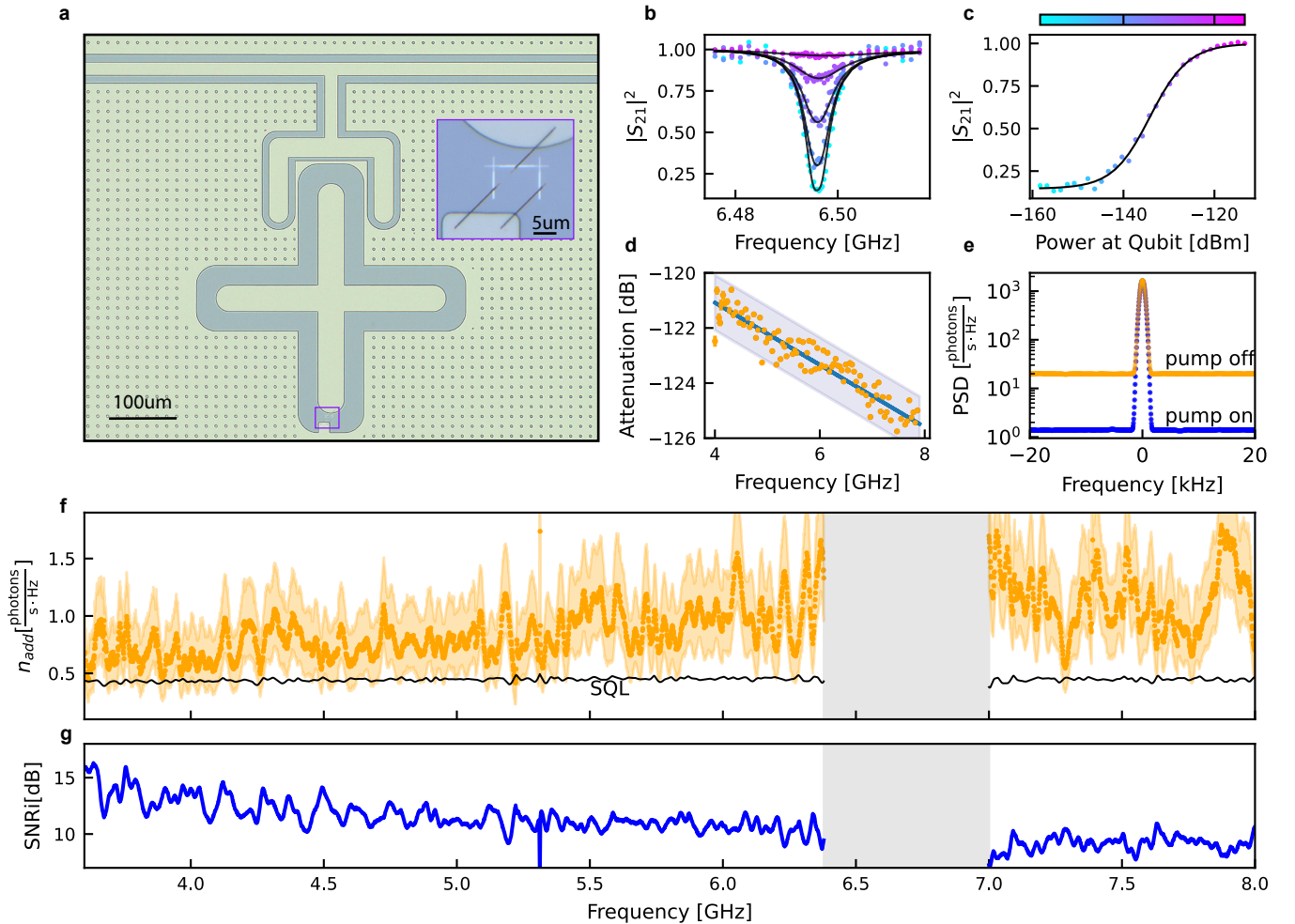


FIG. 3. **Noise performance of the near quantum-limited Josephson junctions based TWPA.** **a**, Optical micrograph of the frequency-tunable waveguide transmon used for signal and pump power calibration. The inset shows a magnified view of the SQUID. **b**, Transmittance ($|S_{21}|^2$) of the qubit feedline at varying driving powers. At low power, the resonance indicates the qubit is strongly overcoupled to the feedline. Solid lines represent a global complex fit. **c**, Power dependence of the feedline transmittance on resonance with the qubit. The solid line indicates the fit. **d**, Signal line attenuation extracted across the 4 to 8 GHz qubit tuning range, utilizing the calibrated power at the qubit. The attenuation exhibits a linear frequency dependence in dB (solid line indicates linear fit, shaded blue area indicates ± 1 dB deviation from the linear fit). **e**, Calibrated power spectral density (PSD) of a 5 GHz signal, measured with the parametric pump turned on and off. **f**, Calibrated added noise (n_{add}) in units of photons (solid orange points), with the shaded region representing the measurement uncertainty. The standard quantum limit (SQL, solid black line) accounts for the frequency-dependent parametric gain. The greyed-out band indicates the frequency range where the phase-matching stopband on either the signal or idler inhibits amplification. **g**, Signal-to-noise ratio improvement (SNRi), determined by subtracting the baseline transmission through a bypass cable from the amplified transmission.

metric oscillation, as the amplifier is pushed toward saturation. Consequently, the optimal operating point for the TWPA is chosen to strictly maximize SNRi rather than absolute gain. In Fig. 2, we operate at this SNRi-optimized point, indicated by the dashed black line.

In Fig. 4b we report the output power of various intermodulation products generated by two tones centered at 5 GHz with a 5 MHz separation, plotted against their input power. The ratio of the signal to the intermodulation products decreases rapidly with increasing input power. At low input powers, the signal exceeds the in-

termodulation products by 40 dB. However, near the amplifier's saturation point, this margin narrows to 10 dB, making intermodulation distortion a non-negligible factor for readout fidelity. Extrapolating this trend yields a third-order intercept point (IP3) of approximately -90 dBm, which is 10 dB higher than the measured 1 dB compression point of -100 dBm at this frequency.

In Fig. 4c, we report the 1 dB compression point, the power at which the gain drops by 1 dB from its small-signal value, across the operational frequency range. Finally, Fig. 4d shows the 5° phase distortion point, de-

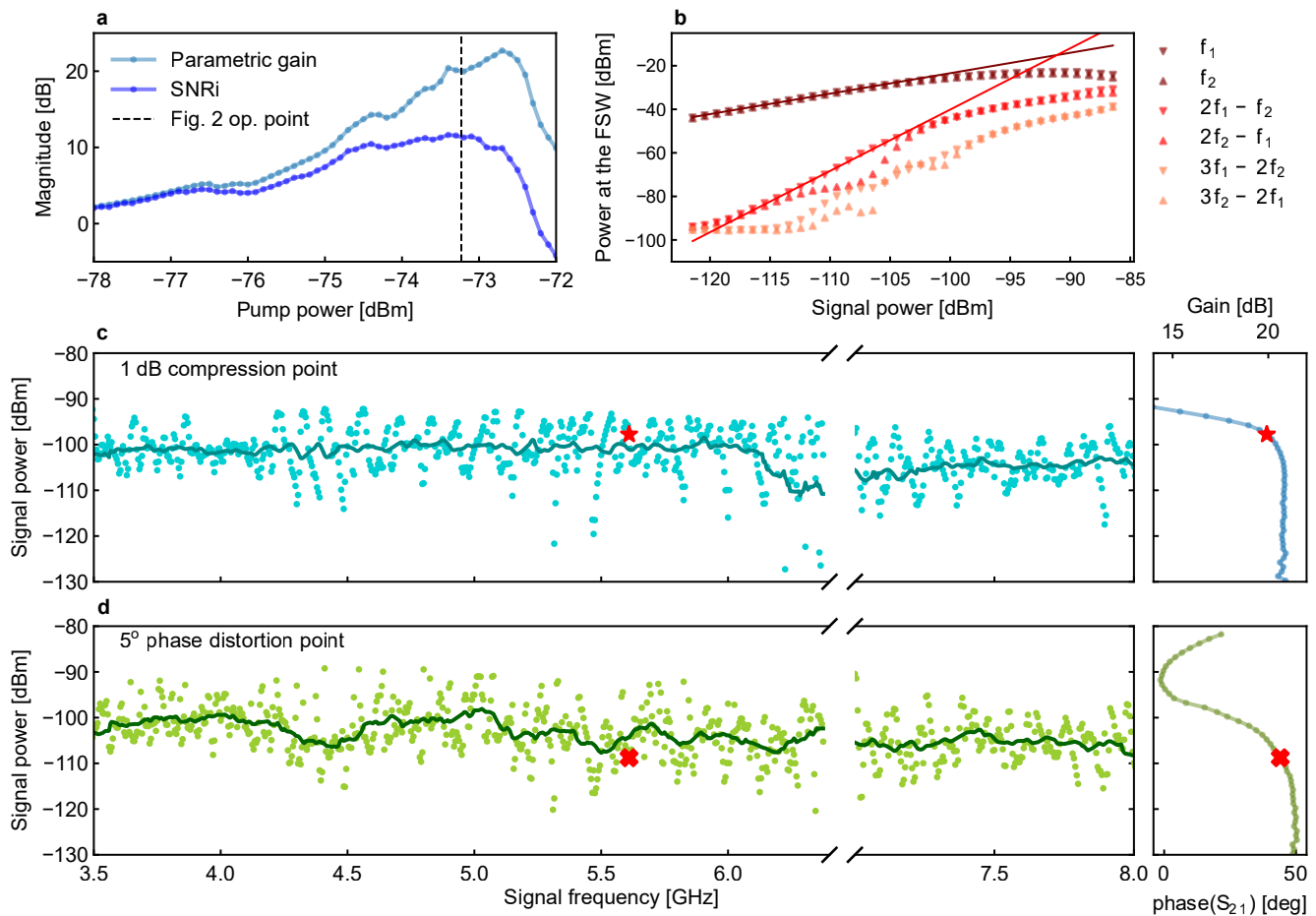


FIG. 4. **Power handling of the amplifier** **a**, Small signal gain and signal-to-noise ratio improvement versus pump power at the input of the amplifier. **b**, Measured powers of different intermodulation products of two tones centered at 5GHz and separated by 5MHz versus their power at the input of the amplifier. **c**, Amplifier 1dB compression point for various signal frequencies within the operational range of frequencies **d**, 5° phase distortion point, i.e. power at which the phase of the amplified signal is shifted 5° with respect to the phase of a small signal at the same frequency.

defined as the input power that induces a 5° phase shift in the amplified signal (relative to the VNA local oscillator) compared to the small-signal phase response. Both the 1 dB compression point and the 5° phase distortion point remain close to -100 dBm across all measured frequencies. This provides a substantial power margin for typical dispersive readout scenarios, where the signal power arriving from a single resonator is roughly -130 dBm, comfortably enabling the simultaneous readout of multiple qubits before saturation effects occur.

Discussion and Conclusion

Our TWPA demonstrates near-quantum-limited performance over an instantaneous bandwidth of approximately 3 GHz, spanning from 3.5 to 6.5 GHz. The residual ripple in the added-noise spectrum mirrors the oscillations in the gain profile, suggesting that both originate from the same nonidealities. By measuring the am-

plification performance with -10dB attenuators placed immediately before and after the sample packaging, we observed a reduced ripple amplitude, but no significant overall improvement in amplification. Therefore, while a baseline impedance mismatch between the TWPA and the 50Ω environment is present, consistent with the estimated 58.5Ω transmission line impedance, it can be ruled out as the primary source of these nonidealities. Instead, the observed behavior may be attributed to the scattering of the junctions' critical currents among individual unit cells, which aligns with the geometrical variation of the junction areas across different positions on the chip. This identifies junction fabrication as the key target for further improvement, specifically through the optimization of the lithography process and transitioning to a fully DUV-defined architecture [12, 30, 31].

The measured 1 dB compression point above -102 dBm is compatible with circuit-QED multiplexed dispersive readout with single readout tone power around -130 dBm. Relative to the previous implementations of resonantly

phase-matched TWPAs, including the device reported in [12] or photonic crystal TWPAs [32], our amplifier achieves a similar gain and bandwidth with substantially lower insertion loss. This is an important practical advantage, since low off-state loss reduces degradation of the measurement chain when the amplifier is not pumped. Compared with more recent low-loss resonant phase matching TWPAs implementations [22] on $5 \times 40 \text{ mm}^2$ chips, the present device is competitive in gain and bandwidth while offering a footprint of $6.6 \times 6.6 \text{ mm}^2$.

The central advance of this work is therefore not a single extreme performance metric, but rather the combination of near-quantum-limited operation, low insertion loss, compact footprint, and compatibility with wafer-level planar fabrication. These results support compact resonantly phase-matched TWPAs as a credible route toward scalable cryogenic microwave hardware and frequency-multiplexed readout. Further progress should be possible by extending the fabrication flow toward deep-UV-defined Josephson junctions, in line with processes already developed at the industrial level for superconducting qubit technologies.

Author Contributions

M.S., H.L. and E.G. designed the experiment. H.L. designed the sample with the input from M.S. . H.L. developed the fabrication process with input from E.G. and M.S. . H.L. fabricated the samples. E.G. and H.L. took the measurements reported in the manuscript. H.L., E.G. and M.S. analyzed the data. S.H. and K.H. designed, assembled and tested the sample packaging. T.J.K. supervised the project. E.G., M.S. and H.L. wrote the manuscript with input from all authors.

Acknowledgement

We thank Mahdi Chegnizadeh for realizing gold CPWs and measuring packaging scattering and Shingo Kono for insightful discussions. This work was supported by Innosuisse via the International project 119.473 INT-ENG (Q-LAEP), by the EU Horizon Europe research and innovation programme under grant No. 101248749 (QuAMP) and by EPFL via the QTNet initiative. M.S. acknowledges support from the EPFL Center for Quantum Science and Engineering postdoctoral fellowship. This work was also supported by the Korea Institute for Advancement of Technology (KIAT) grant funded by the Korea Government (MOTIE) (Quantum LAEP: Quantum Limited Amplifiers with Engineered Pump, Project No. P0028266). The device was fabricated in the Center of MicroNanoTechnology (CMi) at EPFL, and the packaging was realized by WithWave.

-
- [1] A. A. Clerk, M. H. Devoret, S. M. Girvin, F. Marquardt, and R. J. Schoelkopf, Introduction to quantum noise, measurement, and amplification, *Reviews of Modern Physics* **82**, 1155 (2010).
 - [2] J. Aumentado, Superconducting parametric amplifiers: The state of the art in Josephson parametric amplifiers, *IEEE Microwave Magazine* **21**, 45 (2020).
 - [3] M. A. Castellanos-Beltran, K. Irwin, G. Hilton, L. Vale, and K. Lehnert, Amplification and squeezing of quantum noise with a tunable Josephson metamaterial, *Nature Physics* **4**, 929 (2008).
 - [4] R. Vijay, D. Slichter, and I. Siddiqi, Observation of quantum jumps in a superconducting artificial atom, *Physical Review Letters* **106**, 110502 (2011).
 - [5] A. Roy and M. Devoret, Introduction to parametric amplification of quantum signals with Josephson circuits, *Comptes Rendus Physique* **17**, 740 (2016).
 - [6] J. Y. Mutus, T. C. White, R. Barends, Y. Chen, Z. Chen, B. Chiaro, A. Dunsworth, E. Jeffrey, J. Kelly, A. Megrant, *et al.*, Strong environmental coupling in a Josephson parametric amplifier, *Applied Physics Letters* **104**, 263513 (2014).
 - [7] C. Eichler and A. Wallraff, Controlling the dynamic range of a Josephson parametric amplifier, *EPJ Quantum Technology* **1**, 2 (2014).
 - [8] A. Cullen, A travelling-wave parametric amplifier, *Nature* **181**, 332 (1958).
 - [9] P. K. Tien, Parametric amplification and frequency mixing in propagating circuits, *Journal of Applied Physics* **29**, 1347 (1958).
 - [10] O. Yaakobi, L. Friedland, C. Macklin, and I. Siddiqi, Parametric amplification in Josephson junction embedded transmission lines, *Physical Review B* **87**, 144301 (2013).
 - [11] K. O'Brien, C. Macklin, I. Siddiqi, and X. Zhang, Resonant phase matching of Josephson junction traveling wave parametric amplifiers, *Physical Review Letters* **113**, 157001 (2014).
 - [12] C. Macklin, K. O'Brien, D. Hover, M. Schwartz, V. Bolkhovskiy, X. Zhang, W. Oliver, and I. Siddiqi, A near-quantum-limited Josephson traveling-wave parametric amplifier, *Science* **350**, 307 (2015).
 - [13] B. Ho Eom, P. K. Day, H. G. LeDuc, and J. Zmuidzinas, A wideband, low-noise superconducting amplifier with high dynamic range, *Nature Physics* **8**, 623 (2012).
 - [14] M. R. Vissers, R. P. Erickson, H.-S. Ku, L. Vale, X. Wu, G. Hilton, and D. P. Pappas, Low-noise kinetic inductance traveling-wave amplifier using three-wave mixing, *Applied Physics Letters* **108**, 012601 (2016).
 - [15] A. B. Zorin, M. Khabipov, J. Dietel, and R. Dolata, Traveling-wave parametric amplifier based on three-wave mixing in a Josephson metamaterial, in *2017 16th International Superconductive Electronics Conference (ISEC)* (IEEE, 2017) pp. 1–3.
 - [16] V. Gaydamachenko, C. Kissling, and L. Grünhaupt, rf-SQUID-based traveling-wave parametric amplifier with input saturation power of 84 dBm across more than one octave in bandwidth, *Physical Review Applied* **23**, 064053 (2025).
 - [17] A. Fadavi Roudsari, D. Shiri, H. Renberg Nilsson,

- G. Tancredi, A. Osman, I.-M. Svensson, M. Kudra, M. Rommel, J. Bylander, V. Shumeiko, *et al.*, Three-wave mixing traveling-wave parametric amplifier with periodic variation of the circuit parameters, *Applied Physics Letters* **122**, 052601 (2023).
- [18] H. R. Nilsson, L. Chen, G. Tancredi, R. Rehammar, D. Shiri, F. Nilsson, A. Osman, V. Shumeiko, and P. Delsing, A small footprint travelling-wave parametric amplifier with a high signal-to-noise ratio improvement in a wide band, arXiv preprint arXiv:2408.16366 [10.48550/arXiv.2408.16366](https://arxiv.org/abs/2408.16366) (2024).
- [19] A. Ranadive, M. Esposito, L. Planat, E. Bonet, C. Naud, O. Buisson, W. Guichard, and N. Roch, Kerr reversal in Josephson meta-material and traveling wave parametric amplification, *Nature Communications* **13**, 1737 (2022).
- [20] M. Bell, Josephson traveling-wave parametric amplifier with inverse Kerr phase matching, *Physical Review Applied* **25**, 014075 (2026).
- [21] K. Peng, M. Naghiloo, J. Wang, G. D. Cunningham, Y. Ye, and K. P. O'Brien, Floquet-mode traveling-wave parametric amplifiers, *PRX Quantum* **3**, 020306 (2022).
- [22] J. Wang, K. Peng, J. M. Knecht, G. D. Cunningham, A. E. Lombo, A. Yen, D. A. Zaidenberg, M. Gingras, B. M. Niedzielski, H. Stickler, *et al.*, High-efficiency, low-loss Floquet-mode traveling wave parametric amplifier, arXiv preprint arXiv:2503.11812 [10.48550/arXiv.2503.11812](https://arxiv.org/abs/2503.11812) (2025).
- [23] C. S. Chang, A. F. Van Loo, C.-C. Hung, Y. Zhou, C. Gnaandt, S. Tamate, and Y. Nakamura, Josephson traveling-wave parametric amplifier based on a low-intrinsic-loss lumped-element coplanar waveguide, *Physical Review Applied* **24**, 044081 (2025).
- [24] M. Esposito, A. Ranadive, L. Planat, S. Leger, D. Fraudet, V. Jouanny, O. Buisson, W. Guichard, C. Naud, J. Aumentado, *et al.*, Observation of two-mode squeezing in a traveling wave parametric amplifier, *Physical Review Letters* **128**, 153603 (2022).
- [25] M. Perelshtein, K. Petrovnin, V. Vesterinen, S. Hamedani Raja, I. Lilja, M. Will, A. Savin, S. Simbierowicz, R. N. Jabdaraghi, J. S. Lehtinen, *et al.*, Broadband continuous-variable entanglement generation using a Kerr-free Josephson metamaterial, *Physical Review Applied* **18**, 024063 (2022).
- [26] J. Y. Qiu, A. Grimsmo, K. Peng, B. Kannan, B. Lienhard, Y. Sung, P. Krantz, V. Bolkhovskiy, G. Calusine, D. Kim, *et al.*, Broadband squeezed microwaves and amplification with a Josephson travelling-wave parametric amplifier, *Nature Physics* **19**, 706 (2023).
- [27] H. Renberg Nilsson, D. Shiri, R. Rehammar, A. Fardavi Roudsari, and P. Delsing, Peripheral circuits for ideal performance of a traveling-wave parametric amplifier, *Physical Review Applied* **21**, 064062 (2024).
- [28] K. Peng, R. Poore, P. Krantz, D. E. Root, and K. P. O'Brien, X-parameter based design and simulation of josephson traveling-wave parametric amplifiers for quantum computing applications, in *2022 IEEE International Conference on Quantum Computing and Engineering (QCE)* (IEEE, 2022) pp. 331–340.
- [29] A. Remm, S. Krinner, N. Lacroix, C. Hellings, F. Swiadek, G. J. Norris, C. Eichler, and A. Wallraff, Intermodulation distortion in a josephson traveling-wave parametric amplifier, *Physical Review Applied* **20**, 034027 (2023).
- [30] J. Van Damme, S. Massar, R. Acharya, T. Ivanov, D. Perez Lozano, Y. Canvel, M. Demarets, D. Vangoidenhoven, Y. Hermans, J. Lai, *et al.*, Advanced cmos manufacturing of superconducting qubits on 300 mm wafers, *Nature* **634**, 74 (2024).
- [31] C.-T. Ke, J.-Y. Tsai, Y.-C. Chen, Z.-W. Xu, E. Blackwell, M. A. Snyder, S. Weeden, P.-S. Chen, C.-M. Lai, S.-S. Sheu, *et al.*, Scaffold-assisted window junctions for superconducting qubit fabrication, arXiv preprint arXiv:2503.11010 [10.48550/arXiv.2503.11010](https://arxiv.org/abs/2503.11010) (2025).
- [32] L. Planat, A. Ranadive, R. Dassonneville, J. Pueras Martínez, S. Léger, C. Naud, O. Buisson, W. Hasch-Guichard, D. M. Basko, and N. Roch, Photonic-crystal Josephson traveling-wave parametric amplifier, *Physical Review X* **10**, 021021 (2020).